Check for updates

Macromolecular Materials and Engineering

Macromolecular Materials and Engineering Open Access

www.mame-journal.de

RESEARCH ARTICLE OPEN ACCESS

Flexible and Biodegradable Cellulose Counter-Electrode in Aqueous-Based Dye-Sensitized Solar Cells

Elena Palmieri[1] | Sara Ferrara[2] | Sanchari Chowdhury[2] | Luca Montaina[1] | Claudia Mazzuca[3] | Ruben D. Costa[2] | Luca Maiolo[1] | Francesco Maita[1]

[1]Istituto per la Microelettronica e i Microsistemi, Consiglio Nazionale delle Ricerche, Rome, Italy | [2]Technical University of Munich, Straubing, Germany | [3]Department of Chemical Science and Technologies, University of Rome "Tor Vergata", Rome, Italy

Correspondence: Luca Maiolo (luca.maiolo@cnr.it)

Received: 10 November 2025 | **Revised:** 8 May 2026 | **Accepted:** 13 May 2026

Keywords: aqueous electrolyte | biodegradable cellulose substrate | biodegradable electrodes | dye-sensitized solar cells | flexible counter electrodes | sustainable energy | sustainable photovoltaics

ABSTRACT

Sustainable fabrication of photovoltaic devices remains challenging due to the widespread use of non-renewable substrates and organic solvents. In this work, we investigate biodegradable cellulose-based substrates for flexible counter electrodes in aqueous dye-sensitized solar cells (DSSCs). Ethyl cellulose films prepared from different solvents were characterized in terms of rheology, mechanical flexibility, and biodegradability. The optimized formulation was coated with Ti/Au/Pt catalytic three-layer and integrated into aqueous DSSC devices. The resulting solar cells achieved a maximum power conversion efficiency of 1.06%, comparable to reference devices fabricated on glass substrates using the same architecture. These results demonstrate that biodegradable cellulose substrates can support functional photovoltaic devices, providing a promising pathway toward more sustainable optoelectronic technologies.

1 | Introduction

Photovoltaic technologies are central to the transition toward sustainable energy systems [1, 2]. Alongside established crystalline silicon technologies, increasing attention is being devoted to emerging photovoltaic platforms that enable lightweight, flexible, and solution-processed devices [3, 4]. Among these, dye-sensitized solar cells (DSSCs) represent an attractive architecture due to their relatively simple fabrication, compatibility with alternative substrates, and good performance under diffuse or indoor illumination [5]. However, conventional DSSCs are typically fabricated on rigid conductive glass and rely on organic solvent-based electrolytes, which limits their compatibility with flexible and environmentally sustainable device concepts [6–14].

In this context, the development of renewable and biodegradable materials for electronic and photovoltaic devices has become an active research area. Cellulose-based materials are particularly attractive due to their abundance, low cost, biodegradability, and mechanical flexibility [15–19]. Moreover, cellulose derivatives can be processed into transparent and mechanically robust films, enabling their integration as substrates in flexible electronics. Several studies have explored cellulose-derived materials in optoelectronic devices. Cellulose nanopaper and cellulose nanofibers have been used as substrates in organic photovoltaics (OPVs) and perovskite solar cells (PSCs), often combined with conductive networks such as metallic nanowires or hybrid polymer matrices to improve electrical performance [20–23]. Highly efficient OPVs fabricated on cellulose-based substrates have been reported with efficiencies approaching 18%. However, many of these systems

Elena Palmieri, Sara Ferrara, and Sanchari Chowdhury contributed equally to this work.

This is an open access article under the terms of the Creative Commons Attribution License, which permits use, distribution and reproduction in any medium, provided the original work is properly cited.
© 2026 The Author(s). *Macromolecular Materials and Engineering* published by Wiley-VCH GmbH

rely on composite materials or non-biodegradable components [24–28], partially compromising the environmental benefits of cellulose-based platforms.

The application of cellulose substrates in dye-sensitized solar cells has been explored to a much lesser extent. In some cases, conductive regenerated cellulose electrodes or cellulose-paper-based counter electrodes have been demonstrated, reaching efficiencies ranging from approximately 1% to 8% [29–31]. Nevertheless, these devices typically rely on conventional organic electrolytes and sensitizers, meaning that the overall device architecture still depends on materials and processes with limited environmental compatibility. An alternative strategy toward more sustainable DSSCs involves the use of aqueous electrolytes, which replace volatile organic solvents with water-based systems. Although aqueous DSSCs generally exhibit lower efficiencies, they provide a promising platform for evaluating environmentally compatible device components and fabrication approaches.

In this work, we investigate biodegradable cellulose-based counter electrodes for aqueous DSSCs. Ethyl cellulose (EC) films and EC:HPC blends were prepared using different solvent systems and characterized in terms of morphology, rheological properties of the dispersions, mechanical flexibility, and biodegradability. The optimized substrates were subsequently integrated into DSSC architectures by depositing catalytic Ti/Au/Pt layers to form flexible counter electrodes compatible with aqueous electrolytes. The resulting devices demonstrate that cellulose-based substrates can support functional photovoltaic architectures, achieving efficiencies up to 1.06%, comparable to reference devices fabricated on glass using the same electrode configuration and to other cellulose CE based DSSCs [29, 32]. This work therefore provides a proof-of-concept demonstration of biodegradable substrates for aqueous DSSCs and contributes toward the development of more sustainable photovoltaic technologies.

2 | Results and Discussion

2.1 | Film Formation and Morphology

In a previous study [33], EC and EC:HPC dispersions prepared in ethanol were characterized in terms of rheological behavior and film morphology. Briefly, EC films showed relatively smooth and homogeneous surfaces, whereas EC:HPC films exhibited increased surface roughness and structural heterogeneity due to the coexistence of two polymeric components with different hydrophilicity and chain mobility. UV–Vis measurements revealed that both materials display decreasing transmittance at shorter wavelengths, although EC:HPC films generally show lower transparency due to enhanced light scattering associated with the heterogeneous polymer matrix.

In the present work, the analysis was extended to EC dispersions prepared using different solvent systems, namely ethanol (EtOH-EC), n-butyl acetate (But-EC), and a toluene:ethanol mixture (Tol-EC), in order to evaluate the influence of solvent choice on dispersion behavior and film formation. Representative images of the dispersions and the resulting solvent-cast films are shown in Figure 1 (top, middle). While most dispersions appeared slightly hazy, the Tol-EC formulation exhibited higher transparency, suggesting improved polymer solvation in the mixed solvent system.

Despite these differences in the dispersion phase, the solvent-cast EC films displayed similar optical transparency and surface appearance, as shown in the photographs and optical microscopy images in Figure 1 (middle, bottom). All EC-based films exhibited relatively smooth surfaces with no major morphological defects, whereas the EC:HPC film appeared more heterogeneous and slightly opaque. This difference is consistent with the phase heterogeneity expected in polymer blends containing components with different polarity and solubility characteristics.

To further investigate the behavior of the dispersions prior to film formation, rheological measurements were performed to evaluate their viscoelastic properties (Figure 2, Figure S1). The rheological response of polymer dispersions plays an important role in determining film formation dynamics, since solvent–polymer interactions influence chain mobility, dispersion stability, and drying behavior. Frequency sweep measurements allowed the determination of the storage modulus (G') and loss modulus (G''), which describe the elastic and viscous contributions to the mechanical response of the dispersions, respectively. The EC:HPC dispersion exhibited a more complex viscoelastic profile compared to the EC-only systems, with two crossover points between G' and G''. Such behavior suggests the presence of structural heterogeneity arising from the interaction between ethyl cellulose and hydroxypropyl cellulose chains, which may generate transient network structures within the dispersion [34]. In contrast, EC-only dispersions prepared with the different solvent systems displayed more conventional viscoelastic behavior characterized by a single crossover point between G' and G'' and a progressive increase of both moduli with frequency.

Although the overall rheological behavior of the EC dispersions is similar, the position of the crossover frequency varies depending on the solvent used, indicating differences in polymer–solvent interactions and chain mobility. In particular, dispersions prepared in ethanol exhibited higher viscoelastic moduli, suggesting stronger interchain interactions and a more structured dispersion state, while the Tol-EC system showed lower moduli, consistent with improved polymer solvation and increased chain mobility in the mixed solvent environment [35–39]. A thorough discussion of the rheological features is reported in Section S1). Overall, these results indicate that the solvent choice influences the organization of the cellulose chains in the dispersion phase and consequently affects film formation and mechanical properties of the resulting substrates. In detail, the EC systems prepared with n-butyl acetate and toluene:ethanol mixtures exhibit rheological characteristics compatible with the formation of flexible and cohesive films, making them promising candidates for the fabrication of cellulose-based substrates for optoelectronic devices [40, 41].

2.2 | Mechanical and Electromechanical Stability

The mechanical stability of the cellulose-based substrates is a key parameter for their integration into flexible electronic devices. In particular, the ability of the films to withstand mechanical defor-

14392054, 2026, 7, Downloaded from https://onlinelibrary.wiley.com/doi/10.1002/mame.202500434 by CochraneItalia, Wiley Online Library on [22/10/2026]. See the Terms and Conditions (https://onlinelibrary.wiley.com/terms-and-conditions) on Wiley Online Library for rules of use; OA articles are governed by the applicable Creative Commons License

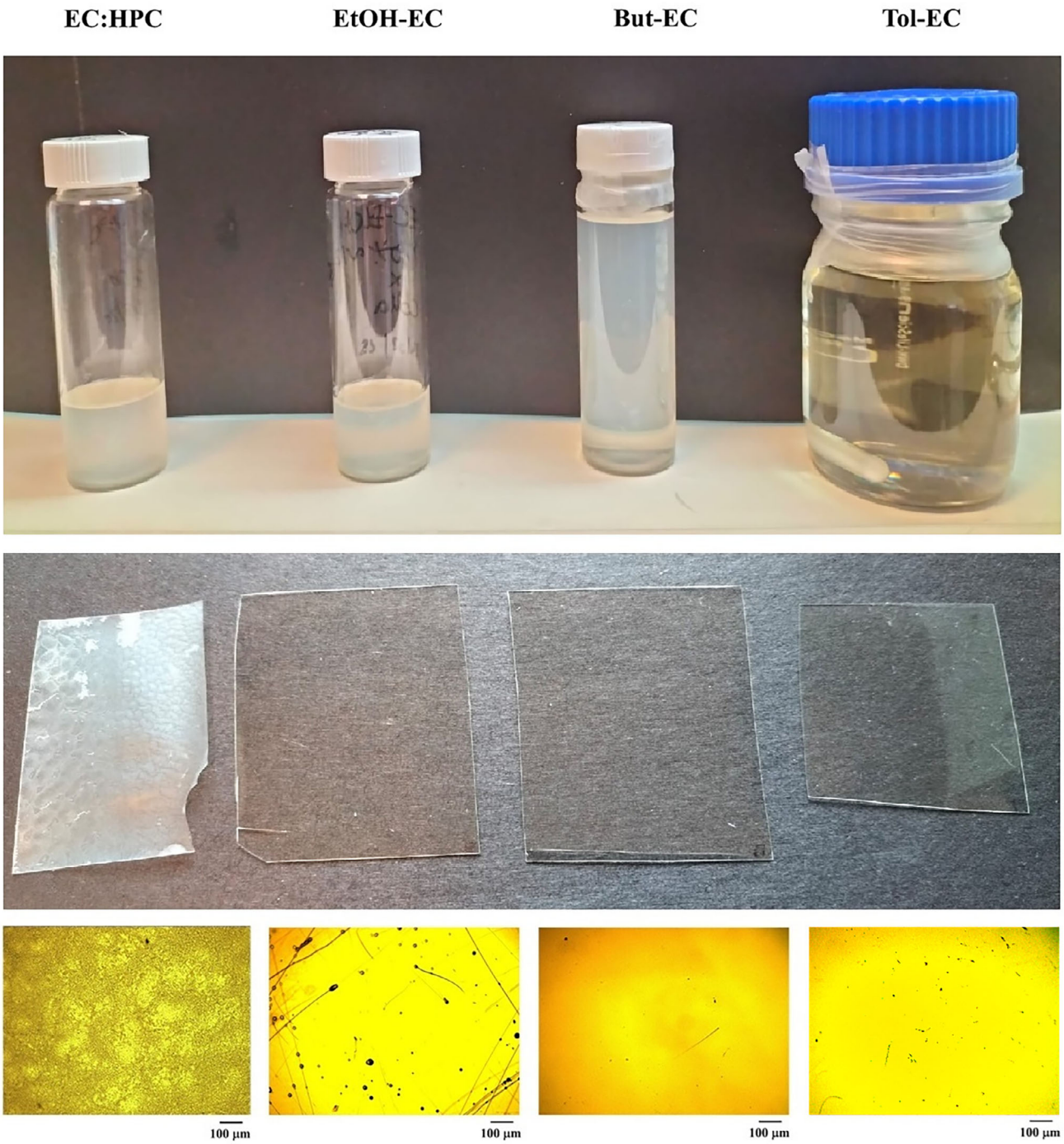


FIGURE 1 | Top: Images of the four cellulose-based dispersions examined in this study. Middle: Photographs of the corresponding solvent-cast films. Bottom: Optical microscopy images of the films showing the surface morphology of each film.

mation without significant degradation of electrical properties is essential when the materials are used as substrates for conductive electrodes.

To evaluate the mechanical behavior of the different formulations, tensile strain tests and cyclic bending experiments were performed (Figure 3, Figure S2). The strain tests revealed clear differences among the investigated substrates depending on the solvent used during film preparation. The Tol-EC and But-EC substrates exhibited comparable mechanical behavior, showing elongation at break values of 8.7 ± 2.3% and 8.3 ± 1.7%, respectively. These values indicate good flexibility and mechanical robustness of the films. In contrast, EtOH-EC films displayed significantly lower elongation (1.2 ± 0.1%), suggesting a more brittle behavior. The EC:HPC blend exhibited intermediate performance, reaching an elongation of 3.2 ± 1.2%.

In addition to the tensile tests, cyclic bending experiments were performed to evaluate the electromechanical stability of the films under repeated deformation. In these measurements,

14392054, 2026, 7, Downloaded from https://onlinelibrary.wiley.com/doi/10.1002/mame.202500434 by CochraneItalia, Wiley Online Library on [22/10/2026]. See the Terms and Conditions (https://onlinelibrary.wiley.com/terms-and-conditions) on Wiley Online Library for rules of use; OA articles are governed by the applicable Creative Commons License

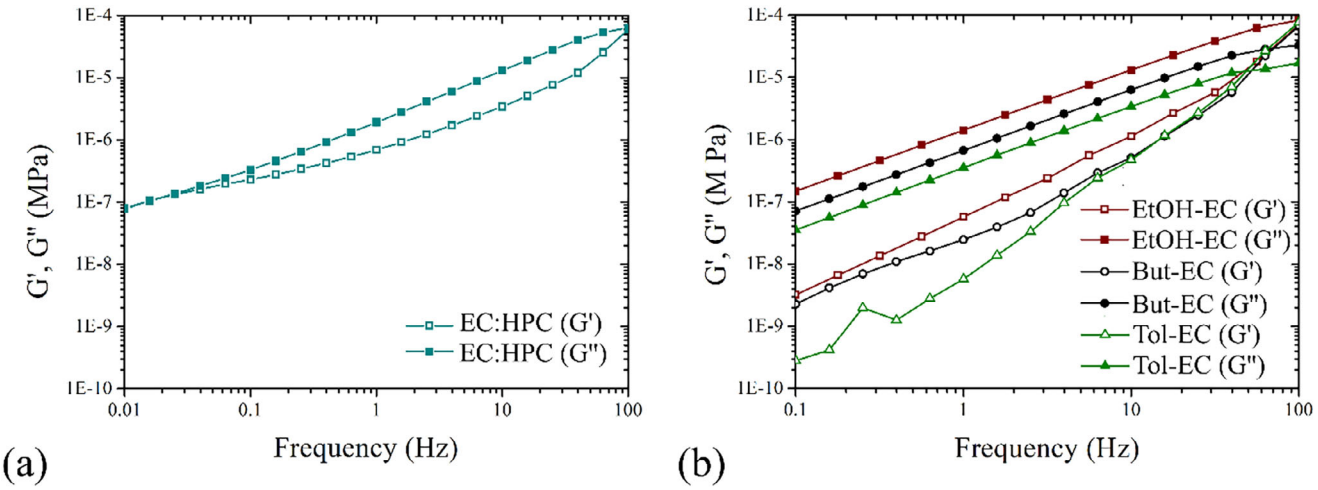


FIGURE 2 | Frequency sweep rheological analysis of the cellulose dispersions. (a) Storage modulus (G') and loss modulus (G'') as a function of frequency for the EC:HPC dispersion in ethanol. (b) G′ and G″ of EC dispersions prepared with different solvents (ethanol, n-butyl acetate, and a toluene:ethanol mixture) namely EtOH-EC, But-EC and Tol-EC.

the variation of the electrical resistance was monitored during 1000 bending cycles. EtOH-EC films could not achieve an end-to-end distance of less than 2 cm without breaking [33], the Tol-EC and But-EC and the EC:HPC films readily accommodated such distances (Figure S2a–c). Therefore, for consistency and comparability, all substrates were tested at an end-to-end distance of 2 cm (Figure S2d).

The EtOH-EC substrates showed the poorest performance under cyclic deformation (Figure 3g). During bending cycles, the relative resistance variation exceeded 100%, indicating severe mechanical damage and poor electrical stability. Moreover, large fluctuations between the bent and unbent states were observed, suggesting irreversible damage of the conductive layer due to damage of the underlying substrate. In contrast, the Tol-EC and But-EC films exhibited significantly better stability during repeated bending (Figure 3e,f). For Tol-EC films, the resistance variation remained within approximately 6% during the entire test, while But-EC substrates showed a slightly higher increase of around 12%. These relatively small variations indicate good mechanical stability and reversible electrical behavior during deformation. The EC:HPC films showed performance comparable to Tol-EC substrates (Figure 3h), with a maximum resistance variation of approximately 6% during the bending cycles. This result suggests that the polymer blend maintains sufficient mechanical integrity despite the structural heterogeneity observed in the film morphology.

To further investigate the origin of the resistance changes observed during bending tests, the films were analyzed by optical microscopy after completion of the 1000 bending cycles (Figure S3). The images reveal the presence of cracks in the metallic coating in the regions subjected to maximum mechanical stress. These cracks are responsible for the gradual increase in electrical resistance observed during the cyclic deformation tests. Among the different substrates, the EtOH-EC films showed the most severe damage, with pronounced cracking and areas where the metal layer was partially delaminated from the substrate. In contrast, the Tol-EC and But-EC films exhibited only superficial cracking, while the conductive layer remained largely adhered to the substrate. The EC:HPC samples also displayed localized damage, although the overall integrity of the electrode was preserved. The mechanical behavior observed for the different substrates can be correlated with the rheological properties of the precursor dispersions discussed in Section 2.1. In particular, dispersions prepared using ethanol showed higher viscoelastic moduli, indicating stronger interchain interactions and reduced polymer mobility. This behavior likely leads to the formation of more rigid and brittle films upon solvent evaporation. Conversely, the But-EC and Tol-EC systems exhibit lower viscoelastic moduli, suggesting increased chain mobility during film formation, which ultimately results in more flexible and mechanically resilient substrates.

Overall, the results demonstrate that cellulose films prepared from n-butyl acetate and toluene–ethanol solvent systems exhibit superior mechanical stability and electromechanical performance compared to ethanol-based films. These properties make them more suitable for use as flexible substrates for the fabrication of cellulose-based counter electrodes.

2.3 | Biodegradability of Cellulose Substrates

In addition to mechanical robustness required for device fabrication, the biodegradation of such substrates was investigated.

Although cellulose derivatives are generally considered biodegradable materials, their degradation behavior strongly depends on the degree of substitution, polymer structure, and environmental conditions [42, 43]. Chemical modification of cellulose chains and the presence of additives can significantly alter degradation kinetics and mechanisms. Therefore, evaluating the biodegradability of modified cellulose systems is essential when proposing them as environmentally sustainable substrates for electronic devices. In this work, the biodegradation behavior of the cellulose-based substrates was investigated under different environmental conditions including water, soil, enriched

14392054, 2026, 7, Downloaded from https://onlinelibrary.wiley.com/doi/10.1002/mame.202500434 by CochraneItalia, Wiley Online Library on [22/10/2026]. See the Terms and Conditions (https://onlinelibrary.wiley.com/terms-and-conditions) on Wiley Online Library for rules of use; OA articles are governed by the applicable Creative Commons License

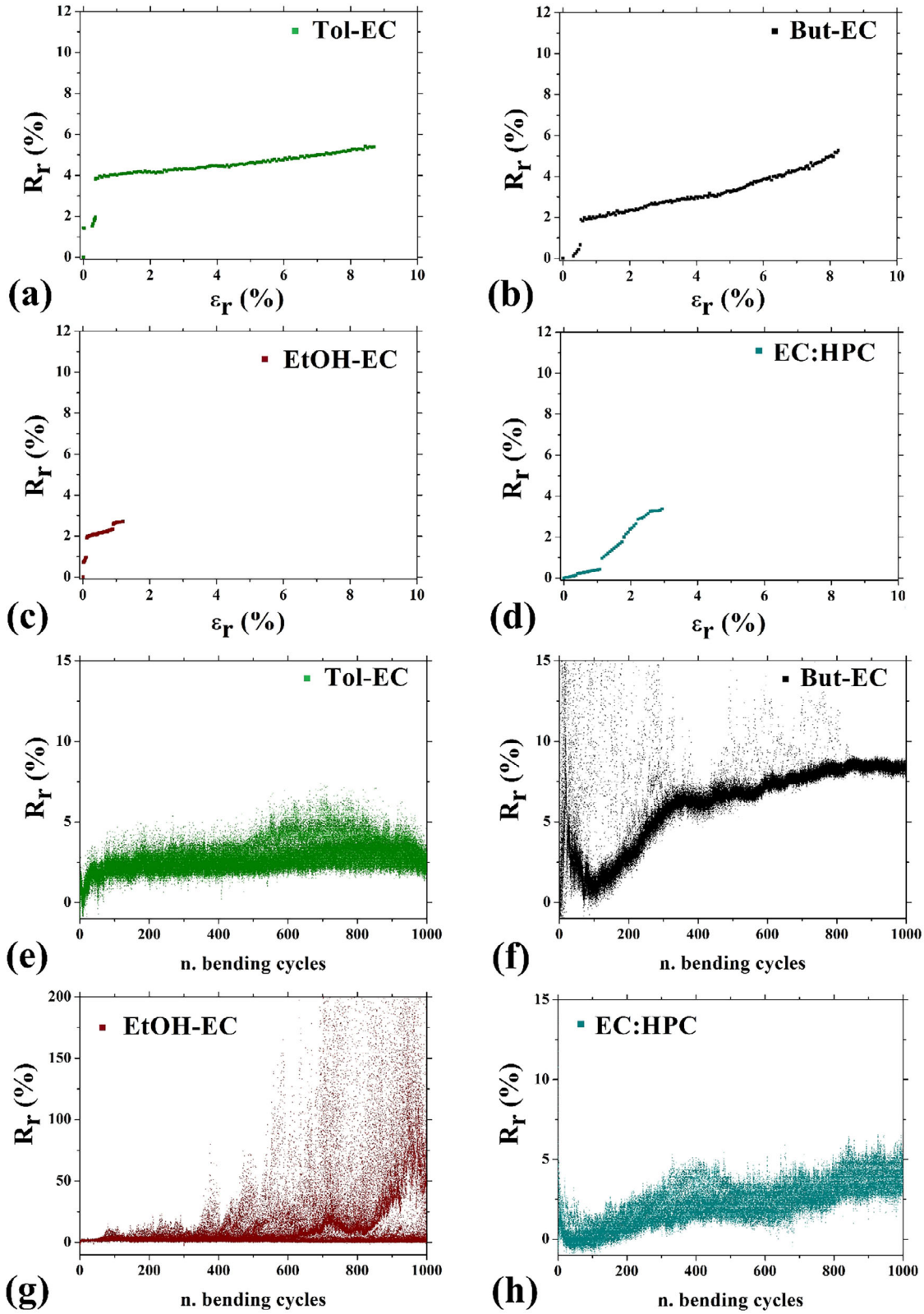


FIGURE 3 | (a–d) Strain test and (e–h) bending test performed on Tol-EC, But-EC, EtOH-EC and EC:HPC respectively.

soil, and home-made compost, based on different standards and general accepted guidelines for the classifications of biodegradable materials [44, 45]. The degradation process was monitored through weight loss measurements over extended periods together with spectroscopic analysis aimed at identifying chemical changes occurring during the degradation process.

Regarding water immersion tests (Figure S4a), the EC substrates remained stable and showed no evidence of swelling, dissolution,

14392054, 2026, 7, Downloaded from https://onlinelibrary.wiley.com/doi/10.1002/mame.202500434 by CochraneItalia, Wiley Online Library on [22/10/2026]. See the Terms and Conditions (https://onlinelibrary.wiley.com/terms-and-conditions) on Wiley Online Library for rules of use; OA articles are governed by the applicable Creative Commons License

or weight loss over time. In contrast, EC:HPC films exhibited rapid water uptake due to the hydrophilic nature of the HPC component, resulting in a noticeable change in texture shortly after immersion. Despite this interaction with water, the samples did not undergo significant degradation under these conditions.

More substantial degradation was observed under soil exposure (Figure S4b,c). Both EC and EC:HPC films remained relatively stable during the initial stages, followed by progressive degradation at longer times. All samples eventually reached complete degradation within approximately two years. The EC samples prepared using different solvent systems exhibited similar degradation profiles, reaching approximately 50% weight loss after about 500 days. In contrast, the EC:HPC films degraded significantly faster, which can be attributed to the higher water permeability introduced by the HPC component, facilitating water diffusion and microbial activity within the polymer matrix.

The degradation process was considerably accelerated under compost conditions. As shown in Figure 4, the EC-based films reached approximately 90% degradation within ten months, while EC:HPC films degraded even faster, achieving nearly complete degradation within about six months. The faster degradation observed in the EC:HPC samples is consistent with the higher hydrophilicity of the blend, which promotes water uptake and microbial colonization.

To gain insight into the chemical processes occurring during degradation, UV–Vis and FT-IR characterizations were carried out for samples treated in home-made compost. The UV–Vis spectra (Figure 5a,b and Figure S5a) show that EC substrates maintain their transparency for extended periods before gradually losing transparency as degradation progresses. In contrast, EC:HPC substrates exhibit a rapid decrease in transparency during the early stages of exposure, which is consistent with the rapid water uptake observed for this material.

ATR–FTIR analysis provides further information on the chemical transformations occurring during degradation. The spectrum of pristine EC (Figure S5b) shows the characteristic absorption bands of the polymer. Notably, in the fingerprint region between 1500 cm^{-1} and 900 cm^{-1}, the spectrum displays prominent peaks corresponding to C–C stretching vibrations, CCH and OCH deformation, and HCH bending as well as from stretching of the C–O–R group (in which R is the ethyl substitution moiety with respect to pure cellulose). Finally a low intense band at about 3400 cm^{-1} is attributable to OH stretching [46–48]. During the degradation process, significant spectral changes are observed. (Figure 5c). In particular, the progressive increase of the band at approximately 1730 cm^{-1} indicates the formation of carbonyl groups, which can be associated with oxidative processes occurring in the cellulose chains. At the same time, the bands at around 3400 and 1640 cm^{-1} become more pronounced, indicating increasing water adsorption within the polymer matrix [49–53].

More interesting, two bands localized at about 1670 and 1540 cm^{-1} evolved (Figure S5c). They are related to the Amide I and II bands, attributable mainly to the C═O stretching and NH bending of the peptide bond in proteins [54, 55]. The appearance of these bands suggests the presence of microbial activity on the polymer surface, indicating that biodegradation involves biological processes occurring within the compost environment. Similar trends were observed for the EC:HPC samples (Figure 5d and Figure S5c,d), where oxidation processes and increased water adsorption are also detected during aging. The presence of the HPC component promotes faster water uptake, which likely facilitates microbial colonization and accelerates degradation. Therefore, the biodegradation of all the cellulose samples in compost involved presumably a multifaceted process that encompassed both hydrolytic cleavage of cellulose bonds [56], likely mediated by cellulolytic enzymes, such as cellulases, and oxidative reactions driven by the interaction with organic matter present in the composting environment. These oxidative processes likely contributed to the breakdown of cellulose chains by generating reactive species, which complemented enzymatic hydrolysis, resulting in a synergistic mechanism of degradation.

The overall results confirm that the investigated cellulose films combine mechanical stability during device operation with the ability to undergo environmental degradation under composting conditions, making them promising substrates for sustainable electronic devices.

2.4 | Fabrication of Cellulose-Based Counter Electrodes

In light of the of the biodegradability and electromechanical results, we decided to fabricate solar cells with the But-EC and EC:HPC films. Among the EC-based materials, Tol-EC showed the best mechanical performance during electromechanical testing, closely followed by But-EC. However, due to the higher toxicity and carcinogenicity of toluene, its use was not considered suitable. Although EtOH-EC represents a greener option in terms of solvent sustainability and faster biodegradation, its mechanical properties were inadequate for device fabrication. Therefore, n-butyl acetate was selected as a compromise between mechanical performance and environmental considerations. While classified as a volatile organic solvent, it presents moderate toxicity and good compatibility with ethyl cellulose processing. Future work will explore more sustainable solvent systems to further improve the environmental profile of the fabrication process. As for EC:HPC, although its mechanical properties are slightly inferior to those of Tol-EC and But-EC, this film outperformed EtOH-EC and feature the best biodegradability, warranting its evaluation in the solar cells. Hence, our final selection prioritizes a balance between performance, environmental sustainability, and safety.

DSSCs were fabricated using FTO/TiO_2(13 μm)/D131 photoanodes, aqueous electrolyte (I_3^-/I^-) and step-by-step optimized counter-electrodes (steps summarized in Figure S7 and layout shown in Figure S8) combining But-EC and EC:HPC substrates with multilayered Ti/Au/Pt coatings of different thicknesses for each layer as well as different deposition techniques. The current–voltage (*J–V*) curves were measured under 1 sun AM1.5G conditions—see experimental section for more details.

At first, the But-EC and EC:HPC counter electrodes were fabricated with Ti(25 nm)/Pt(50 nm) coatings via thermal

14392054, 2026, 7, Downloaded from https://onlinelibrary.wiley.com/doi/10.1002/mame.202500434 by CochraneItalia, Wiley Online Library on [22/10/2026]. See the Terms and Conditions (https://onlinelibrary.wiley.com/terms-and-conditions) on Wiley Online Library for rules of use; OA articles are governed by the applicable Creative Commons License

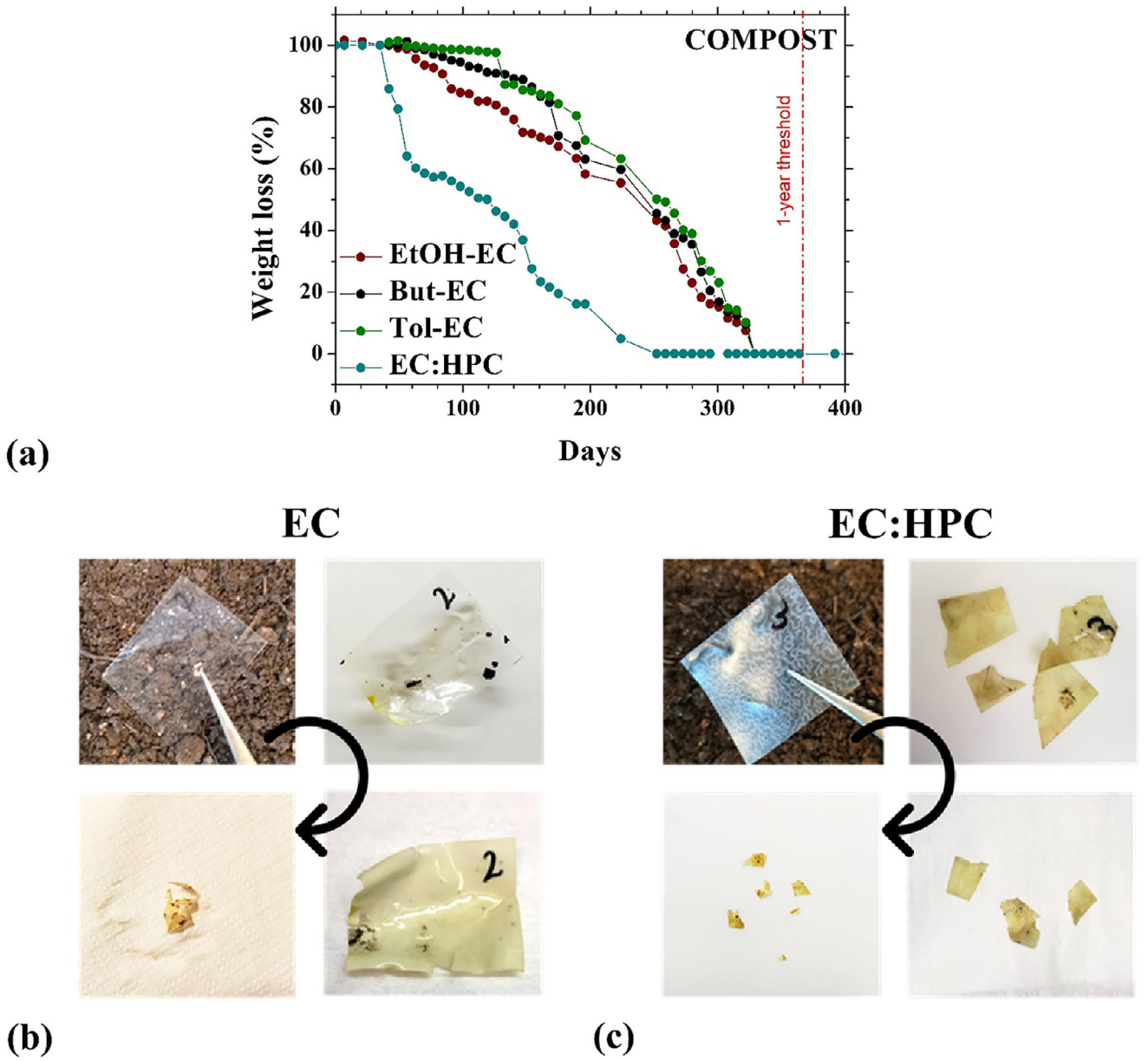


FIGURE 4 | (a) Weight loss for the various substrates (EtOH-EC, But-EC, Tol-EC and EC:HPC) disposed in home-made compost. Images of (b) EC and (c) EC:HPC samples at different degradation time.

deposition—see experimental section. The Ti layer typically enhances the adhesion of the metallic layers, such as the catalytic Pt layer used to regenerate the aqueous electrolyte. Unfortunately, optical microscopy inspection of the electrodes showed the presence of cracks on the metal surface upon deposition of Ti layer (Figure S9a,c, along with a comparison with non-cracked metal in Figure S9b,d). This is likely related to thermal stress during metal deposition, which induces imperfections in the cellulose substrates that can be easily transferred to the thin Pt top layer, potentially impacting device performance. Additionally, the 50 nm Pt layer appeared to cause further damage to the cellulose materials, which showed a very slight wrinkling on the edges, also attributable to thermal stress (Figure S9e). Indeed, the sheet resistance (R_{sheet}) for But-EC/Ti/Pt and EC:HPC/Ti/Pt electrodes is very high, accounting to mean values 27 and 23 Ω €$^{-1}$ respectively. This is associated to a standard deviation of ca. 25%, as expected by the cracked surface morphology. To enhance the overall conductivity of the metal stack minimizing ohmic losses, an intermediate gold (Au) layer of 25, 50, and 75 nm was incorporated together with the optimization of the Ti layer thickness (i.e., 15 nm) and Pt thickness preliminarily set as 10 nm. In these samples, the R_{sheet} significantly reduced to values <5 Ω €$^{-1}$ for both But-EC/Ti/Au/Pt and EC:HPC/Ti/Au/Pt electrodes—Table S1. These values were significantly lower than the commercial ITO-PET substrates (15 Ω €$^{-1}$, Xinyan Technology Ltd.) and configurations base on FTO, Pt-FTO, and graphene/PET [57].

Thus, we integrated these electrodes in the above device architecture. In line with the literature of aqueous DSSCs with D131 [32], devices showed a short-circuit current density (J_{sc}) of 3.17 mA cm^{-2}, open-circuit voltage (V_{oc}) of 452 mV, and a

14392054, 2026, 7, Downloaded from https://onlinelibrary.wiley.com/doi/10.1002/mame.202500434 by CochraneItalia, Wiley Online Library on [22/10/2026]. See the Terms and Conditions (https://onlinelibrary.wiley.com/terms-and-conditions) on Wiley Online Library for rules of use; OA articles are governed by the applicable Creative Commons License

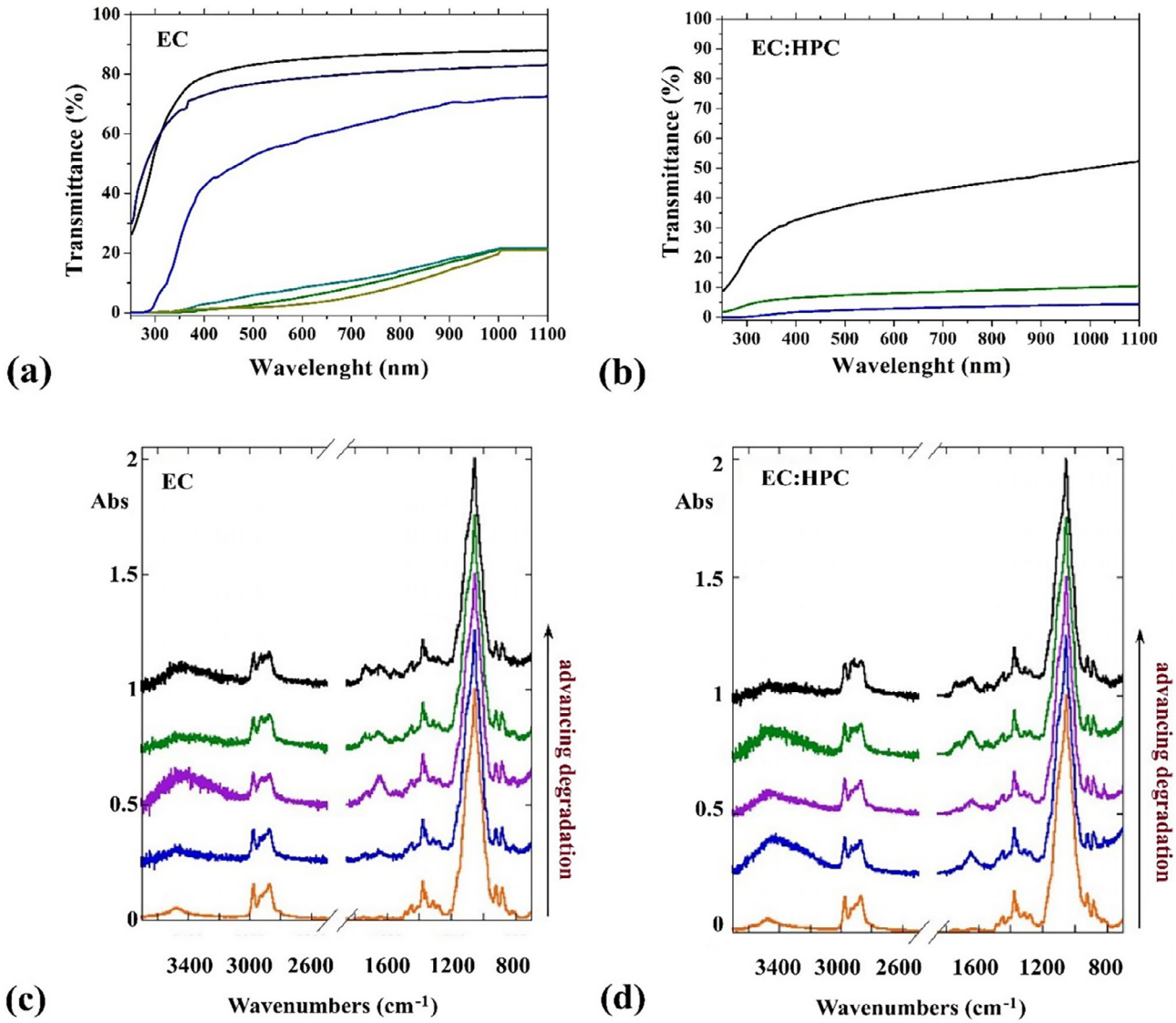


FIGURE 5 | (a) UV–Vis spectra of EC at various stages of degradation. The EC material maintains its transparency for an extended period, with a gradual reduction that coincides with the onset of the degradation process; (b) UV–Vis spectra of EC:HPC at different stages of degradation. In contrast, the EC:HPC material experiences a significant loss of transparency within the first few days, with further deterioration occurring only in the final stages of the degradation process; (c) ATR-FTIR spectra of EC samples over the degradation process; (d) ATR-FTIR spectra of EC:HPC samples over the degradation process. In both cases, bands highlighting oxidation and water adsorption are present. Spectra are normalized to the maximum (at 1050 cm^{-1}) and stacked for clarity.

fill factor (FF) of 52%, resulting in PCE of 0.74% under 1 sun irradiation for devices with the with the thinnest Au interlayer (Table 1 and Figure 6). However, the increase in the Au layer thickness did not exert a significant change on the J_{sc}, while the V_{oc} and *FF* are gradually reduced (Table 1). This suggests that the optimization of the Au layer thickness to enhance electrical conductivity with minimal interference in interfacial charge transfer and ion transport processes for the electrolyte regeneration is important.

Next, we focused on optimizing the thickness of the Pt layer going from 10 nm, to 20 nm and to 40 nm in But-EC substrates. While the increase of Pt layer thickness from 10 to 20 nm did not impact the overall device performance with PCE values of 0.74% and 0.72%, devices with the thickest Pt layer feature a low FF and, in turn, PCE values of 0.56% (Table 2 and Figure 6). This could be related to the formation of a dense layer with reduced surface roughness and fewer accessible catalytic sites for electrolyte regeneration.

2.5 | DSSC Performance and Benchmarking

All the approaches discussed so far share a common drawback: the thermal evaporation process poses challenges for heat dissipation, especially when substrates like cellulose are used. As observed in Figure S9a,c, during thermal evaporation, the cellulose substrate could be unable to efficiently dissipate the accumulated heat, often leading to local overheating. This results in incomplete or uneven metal deposition, which manifests as

14392054, 2026, 7, Downloaded from https://onlinelibrary.wiley.com/doi/10.1002/mame.202500434 by CochraneItalia, Wiley Online Library on [22/10/2026]. See the Terms and Conditions (https://onlinelibrary.wiley.com/terms-and-conditions) on Wiley Online Library for rules of use; OA articles are governed by the applicable Creative Commons License

TABLE 1 | Figures-of-merit of devices fabricated with the counter-electrodes based on But-EC and EC:HPC substrates with different Au layer thickness of 25, 50, and 75 nm.

Counter-electrode configuration	J_{sc} (mA cm^{-2})	V_{oc} (mV)	FF (%)	PCE (%)
But-EC-15/25/10	3.17	452	52	0.74
But-EC-15/50/10	3.13	395	41	0.51
But-EC-15/75/10	3.16	354	52	0.58
EC:HPC-15/25/10	3.34	383	46	0.59
EC:HPC-15/50/10	3.20	307	48	0.47
EC:HPC-15/75/10	2.46	242	36	0.21

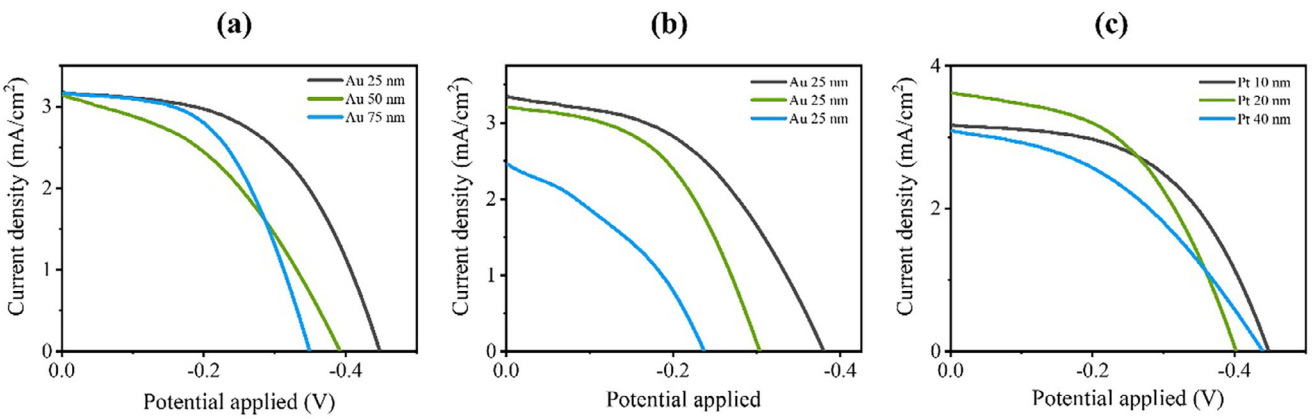


FIGURE 6 | *J-V* curves under 1 sun illumination of the DSSCs with: (a) But-EC/Ti(15 nm)/Au(x nm)/Pt(10 nm), (b) EC:HPC/Ti(15 nm)/Au(x nm)/Pt(10 nm) and (c) But-EC/Ti(15 nm)/Au(25 nm)/Pt(x nm) counter-electrodes (see legend).

TABLE 2 | Figures-of-merit of the devices fabricated with the counter-electrodes based on But-EC substrates with different Pt layer thickness of 10, 20, 40 nm.

Counter-electrode configuration	J_{sc} (mA cm^{-2})	V_{oc} (mV)	FF (%)	PCE(%)
But-EC -15/25/10	3.17	452	52	0.74
But-EC -15/25/20	3.62	405	49	0.72
But-EC -15/25/40	3.09	444	41	0.56

non-uniform, non-mirror-like metallic layers. Such irregularities directly impact the electrical conductivity and interfacial contact of the electrode/electrolyte, ultimately compromising the device's performance.

To mitigate this issue, sputtering has been investigated as an alternative fabrication method. Sputtering allows for better control over deposition parameters and typically enables a more uniform coating, even on thermally sensitive substrates. Here, we conducted sputtering at low power levels to reduce mechanical stress, while maintaining adequate film quality of But-EC. These conditions led to improved adhesion, uniformity, and surface morphology compared to thermally evaporated films. As a proof of concept, we successfully fabricated the optimal counter-electrode composition (But-EC-15/25/20)—see experimental section. In short, the resulting electrodes displayed a mirror-like metallic finish, independent of the specific metal deposited (*e.g.*, Ag or Al), as shown in Figure S9b,d.

Devices fabricated using But-EC/Ti/Au/Pt counter electrodes exhibited an average PCE of 0.94 ± 0.20% (N = 4; Table S2 and Figure S10), with the best-performing device reaching 1.06%, with FF value of 51%, *V*oc of 471 mV, and *J*sc of 4.43 mA/cm^2 (Figure 7 and Table 3). The PCE is moderate compared to the prior-art cellulose paper-based substrate based DSSCs [29] prepared with organic electrolytes — Table 4 — and in line with state of art non-flexible aqueous-based DSSCs — Table S3, while they are similar to reference devices fabricated with glass substrate based counter-electrodes with the same multilayered architecture. These results confirm that with proper tuning, sputtering can serve as a viable and more reliable deposition technique for fabricating cellulose-based optoelectronic devices. Still the current device architecture relies on noble metal catalytic layers (Ti/Au/Pt). While these metals are commonly employed in DSSCs to ensure efficient electrolyte regeneration, future work will investigate alternative carbon-based or conductive polymer catalysts compatible with biodegradable substrates. Finally, it should be noted that the

14392054, 2026, 7, Downloaded from https://onlinelibrary.wiley.com/doi/10.1002/mame.202500434 by CochraneItalia, Wiley Online Library on [22/10/2026]. See the Terms and Conditions (https://onlinelibrary.wiley.com/terms-and-conditions) on Wiley Online Library for rules of use; OA articles are governed by the applicable Creative Commons License

TABLE 3 | Figures-of-merit of the devices fabricated with the counter-electrodes based on But-EC and glass (G) substrates prepared via sputtering.

Counter-electrodes configuration	J_{sc} (mA cm^{-2})	V_{oc} (mV)	FF (%)	PCE (%)
But-EC-15/25/20	4.43	471	51	1.06
G-15/25/20	3.39	456	52	0.80

TABLE 4 | State-of-the-art cellulose-based and flexible DSSCs.

CE architecture	Dye/electrolyte	PCE [%]	Year	DOI
Biodegradable cellulose	D131/aqueous	1.06	2026	This paper
$CuInS_2$/PEDOT:PSS on cellulose	N3/organic	1.06	2023	[29]
ITO-sputtered regenerated cellulose	N719/organic	8.11	2018	[31]
PEDOT:PSS dispersion in hydroxyethylcellulose	N719/organic	4.21	2017	[58]
PEDOT-impregnated cellulose paper	N719/organic	6.1	2016	[59]
PEDOT/ITO-PEN	N719/organic	8.00	2010	[60]
Pt/ITO-PET	N719/organic	8.46	2012	[61]
Ni/Pt/PI (polymide)	N719/organic	6.90	2011	[62]
Pt/carbon sphere/ITO-PET	YD2-o-C8/organic	9.05	2017	[63]
PANI/ITO-PET	Natural dye/organic	1.03	2026	[64]
Pt/Ti-sputtered film/PEN	JH-1+SQ2/organic	6.31	2018	[65]
PPy/Ni-coated fabric	N719/organic	3.83	2016	[66]
Pt/ITO-PET	N719/organic	2.95	2016	[67]
CDS:PEDOT:PSS/ITO-PET	N3/organic	4.84	2023	[68]
PVA/GO/PEDOT:PSS	Cell not fabricated	n.a.	2026	[69]
Reduced GO cotton fabric on PET	N719/organic	2.59	2026	[70]

PEDOT-PSS−− ; ITO—indium tin oxide; PVA—polyvinyl alcohol; GO—graphene oxide; PET—polyethylenthereftalate; PANI—polyanyline: Ppy—polypyrrole.

device architecture used in this work was not optimized for maximum efficiency. Instead, it was selected to evaluate the compatibility of biodegradable cellulose substrates with aqueous DSSC architectures. The obtained efficiencies therefore represent a proof-of-concept validation, demonstrating that the proposed substrates can support stable electrode deposition and catalytic activity.

Finally, it should be noted that the device architecture used in this work was not optimized for maximum efficiency. Instead, it was selected to evaluate the compatibility of biodegradable cellulose substrates with aqueous DSSC architectures. The obtained efficiencies therefore represent a proof-of-concept validation, demonstrating that the proposed substrates can support stable electrode deposition and catalytic activity.

3 | Conclusion

This work investigated biodegradable cellulose-based materials as flexible substrates for counter electrodes in aqueous dye-sensitized solar cells. Ethyl cellulose (EC) films and EC:HPC blends were prepared using different solvent systems and systematically characterized in terms of morphology, rheological behavior of the precursor dispersions, mechanical stability, and biodegradability. The results show that solvent selection plays a key role in determining the mechanical properties of the resulting films. In particular, EC films prepared using n-butyl acetate and toluene–ethanol mixtures exhibited significantly improved flexibility and electromechanical stability compared to ethanol-based films, enabling their use as substrates for conductive electrodes. Biodegradation studies conducted under soil and composting conditions confirmed that the investigated cellulose materials undergo progressive degradation through combined hydrolytic, oxidative, and microbial processes. Following optimization of the metal deposition process, cellulose-based counter electrodes were successfully integrated into aqueous DSSC architectures. Devices fabricated using the optimized But-EC/Ti/Au/Pt electrodes achieved power conversion efficiencies up to 1.06%, comparable to reference devices fabricated on glass substrates using the same electrode configuration. While the efficiency values are moderate, further work is on-going on optimizing the photoelectrode architecture (including flexible biomaterials) as well as the surface-active area of the counter electrode (i.e., micro structuring, replacing noble metal catalytic layers, etc.) to reduce back electron reactions and increase electrolyte regeneration, respectively. At this stage, this work shows the first step-by-step

14392054, 2026, 7, Downloaded from https://onlinelibrary.wiley.com/doi/10.1002/mame.202500434 by CochraneItalia, Wiley Online Library on [22/10/2026]. See the Terms and Conditions (https://onlinelibrary.wiley.com/terms-and-conditions) on Wiley Online Library for rules of use; OA articles are governed by the applicable Creative Commons License

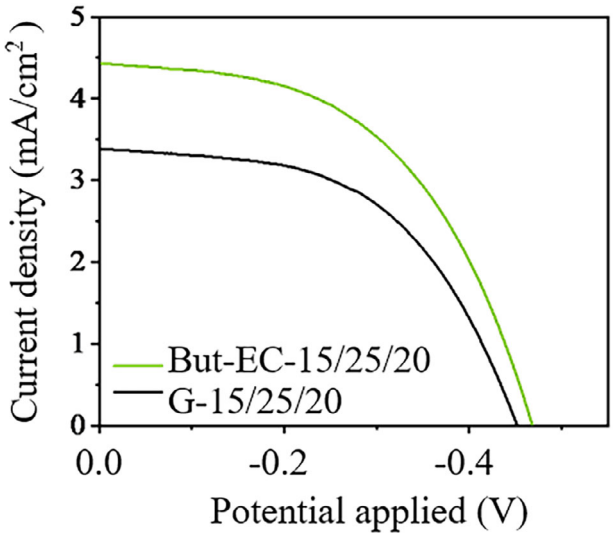


FIGURE 7 | *J–V* curves for DSSCs prepared with G or But-EC/Ti(15 nm)/Au(25 nm)/Pt(20 nm), prepared via sputtering technique.

optimization in metallic layer thickness along with two different substrates gives us better insight in optimization of key DSSC parameters like J_{SC} and $V_{OC.}$ It opens the door to further research work in line of optimizing aqueous electrolyte composition, integration of co-adsorbent materials to achieve higher J_{SC} and V_{OC} with cellulose substrate-based flexible CE in DSSCs.

These findings highlight the potential of cellulose-based materials as environmentally compatible platforms for flexible optoelectronic technologies and represent a step toward the development of more sustainable photovoltaic systems.

4 | Materials and Methods

4.1 | Materials

Hydroxypropyl cellulose (HPC) with MW ≈80.000 Da, ethyl cellulose (EC) with 48–49.5% ethoxy content was purchased from Merck KGaA, Darmstadt, Germany. All the solvents (EtOH, n-butyl acetate, toluene, acetonitrile, 4-tert butanol) used as well as aqueous $TiCl_4$ solution (titanium m(IV) chloride solution, 0.09 M in 20% HCl), iodine (≥99%), sodium iodide (99.9%) and D131 dye (> 95% HPLC), were purchased from Merck. Compost accelerator capsules, which were used to prepare the compost for the biodegradability tests, are obtained from Envii, UK.

FTO glass slides — Pilkington TEC15, 2.2 mm (12–15 ohm sq^{-1}) were purchased from XOP glass. Ti-nanoxide T/SP paste were purchased from Solaronix, Switzerland. 18NR-AO Active opaque TiO_2 paste were purchased from Greatcell-solar.

4.2 | Methods

4.2.1 | Preparations of the Cellulose Substrates

EC was dispersed in three different solvents, and stirred at 45°C until dissolution. EC substrates were prepared via solvent casting from 10%$_{wt}$ solutions on EC dispersed in different solvents: ethanol (EtOH-EC), n-butyl acetate (But-EC), and a mixture of toluene: ethanol 80:20 (Tol-EC). The solutions were cast into a glass container and let dry at room temperature for a period of time ranging from 24 to 168 h depending on the solvent used.

The EC:HPC dispersion (10% wt, HPC ratio 3:1), was prepared by dispersing EC and HPC in ethanol and stirring at 35°C until complete dissolution. The EC:HPC substrates were prepared via solvent casting and let dry at room temperature for 24 h. Then the substrate is removed from the mold with the help of tweezers. In Table 5 the list of substrates fabricated for this study is reported.

4.2.2 | Rheological Characterization of the Polymer Dispersions

Rheological characterization was performed using an HR 20 rheometer by TA Instruments (USA). A cone and plate configuration (steel, 60 mm diameter 2°) was used for all the characterizations.

The viscosity–shear rate profiles of the various dispersions studied, referred to as "flow curves," were determined at 25 °C in a range of shear rates from 0.01 to 1000 s^{-1}. Flow curve graphs are presented as double-logarithmic plots of viscosity (Pa s) vs shear rate (s^{-1}).

Dynamic frequency sweep experiments were performed in the linear viscoelastic region (LVR) of each material with frequencies between 0.1 and 100 Hz, with a 15% strain applied.

All experiments were repeated a minimum of three times, with samples coming from different batches, and in all cases the results were reproduced within a maximum difference of 10%. Errors are not reported in the graphs hereinafter presented for the sake of clarity, and they do not affect the hierarchy of the displayed parameters.

4.2.3 | Biodegradability Study of the Substrate

The biodegradability of the cellulose-based substrates was investigated. In detail, individual material samples measuring 3×6 cm, representing each substrate type, were subjected to four compositing procedures (water, topsoil, enriched soil, and home-made compost, prepared according to guidelines reported in SI) and monitored (depending on the specific degradation medium) up to 700 days as outlined in the following sections.

In short, a batch of the four samples was placed in deionized water, each in a different tank, at room temperature, to study water biodegradability. Another batch of four samples was placed in untreated topsoil within a vase and was positioned outdoors throughout the year to simulate open-field weather conditions. The experiment was started in the autumn season. The third batch of four samples was placed in topsoil enriched with some organic waste (leaves, branches, fruit scrapes). It was also left outdoor, sheltered from heavy rain. For the batches placed in soil

14392054, 2026, 7, Downloaded from https://onlinelibrary.wiley.com/doi/10.1002/mame.202500434 by CochraneItalia, Wiley Online Library on [22/10/2026]. See the Terms and Conditions (https://onlinelibrary.wiley.com/terms-and-conditions) on Wiley Online Library for rules of use; OA articles are governed by the applicable Creative Commons License

TABLE 5 | List of the substrates fabricated and tested in this work.

Cellulose used	Solvent used	Coded name
Ethyl cellulose (EC)	Ethanol	EtOH-EC
Ethyl cellulose (EC)	n-butyl acetate	But-EC
Ethyl cellulose (EC)	Toluene:ethanol = 80:20	Tol-EC
Ethyl cellulose (EC) + hydroxypropyl cellulose (HPC)	Ethanol	EC:HPC

or enriched soil, the specific location of each sample was marked using labelled pipettes, as illustrated in Figure S11.

The fourth set of four samples for each substrate type was placed in containers filled with compost, which was prepared in-house. The organic compost was formulated by mixing organic residues (fruit scrapes, leaves, small branches) and a composter accelerator obtained from Envii. A full description of the procedure and the calculations for the preparation of the compost is reported in the Supporting Information. The samples are periodically extracted from the degradation media for analysis, with the frequency of extraction varying depending on the stage of the degradation process (e.g., weekly or monthly). Characterization efforts are more frequent and detailed during the advanced stages of degradation, whereas in the initial stages, evaluations are performed less frequently. For analysis, the samples were taken out of the degradation medium, rinsed with water, gently blotted with kitchen paper, and dried using compressed air. At each interval, the samples are evaluated for weight loss and when appropriate subjected to FT-IR and UV–Vis spectroscopy to assess any chemical modifications resulting from degradation.

In the case of compost medium, concurrently to the withdrawal of the samples for testing, the compost undergoes turning to homogenize materials that have not yet decomposed, facilitating aeration, and adding new organic waste.

4.2.4 | Chemical Physical Characterization on the Substrates

UV–Vis spectroscopy was conducted using a Perkin Elmer (USA) Lambda 35 UV/Vis spectrometer. Spectra were recorded over a wavelength range of 1100 to 200 nm with a resolution of 4 nm.

FTIR-ATR analysis was performed on a ThermoScientific Nicolet Summit spectrometer (Thermo Scientific Inc., Madison WI, USA) in absorbance mode, using the attenuated total reflectance (ATR) technique with a diamond single-reflection accessory. 32 spectra per scan were collected over the range of 4000 to 400 cm^{-1} at a resolution of 2 cm^{-1}.

4.2.5 | Morphological Characterization of the Substrates

The morphological characterization was carried out using optical Olimpus mx50 microscope and field emission scanning electron microscopy (FE-SEM; Sigma 300 Carl Zeiss, ZEISS AG, Oberkochen, Germany).

4.2.6 | Electromechanical Characterization of the Cellulose Substrate

To evaluate the mechanical stability of the cellulose substrates even after multiple cycles of bending, electromechanical assessments (strain and bending) were carried out with a linear stage stepper motor. Prior to testing, cellulose substrates were coated with a 100 nm layer of aluminum via thermal evaporation to ensure conductivity. Samples were cut into 5 × 0.5 cm pieces for the strain tests, and 5 × 1 cm for bending tests. These samples were mounted on a linear trail, controlled by a Newport sp300 stepper motor (as depicted in Figure S12a), and subjected to tension between two holders, one of which is stationary and the other mobile, at a consistent speed of 2 mm s^{-1}. The movement of the motor was controlled by a custom LabView software, managing both the advancement and retraction of the movable holder. To monitor the variation of the sample electrical resistance, the ends of the sample were connected through a copper foil to a Keithley 2440 Multimeter. The electrical resistance was sampled every 50 ms and recorded using LabView software.

Pictures of the bending tests in different bending phases are reported in Figure S12b–d. For bending tests, we reported the Resistance relative variation (R_r) as a function of the number of bending cycles. For strain measurements, we reported the Resistance relative variation as a function of the strain relative variation (ε_r).

The Resistance relative variation was calculated using Equation 1, while the relative strain was calculated using Equation 2.

$$R_r\ (\%) = \frac{R - R_0}{R_0} \times 100 \quad (1)$$

$$\varepsilon_r\ (\%) = \frac{l - l_0}{l_0} \times 100 \quad (2)$$

where R is the resistance, R_0 is the initial resistance, l is the sample final length and l_0 is the initial length. For each characterization, a minimum of three samples for each type of cellulose was tested.

4.2.7 | Preparation of the Cellulose Counter-Electrodes

A three-layer of Ti/Au/Pt configuration was prepared on the EC:HPC and But-EC substrates as well as glass as reference electrodes via thermal and electron beam evaporation (layout in Figure S8a). The Ti layer (15 nm) was deposited with a rate of 3.0 Å s^{-1}. The Au layer (25, 50, and 75 nm) was deposited at a

14392054, 2026, 7, Downloaded from https://onlinelibrary.wiley.com/doi/10.1002/mame.202500434 by CochraneItalia, Wiley Online Library on [22/10/2026]. See the Terms and Conditions (https://onlinelibrary.wiley.com/terms-and-conditions) on Wiley Online Library for rules of use; OA articles are governed by the applicable Creative Commons License

rate of 6 Å s^{-1}. The top Pt layer (10, 20, and 40 nm) were deposited at a rate of 1.5 Å s^{-1}. Since Ti and Pt are high-melting materials deposited via e-gun evaporation, we controlled the growth rate by adjusting the power required for deposition. This approach prevented excessive thermal stress on the cellulose substrate. Finally, we also explored an alternative method via sputtering (power of 500 W, pressure of 500 mTorr under a flux of Argon) to reduce the thermal stress on the cellulose substrates. The sheet resistance of the substrates was measured with Ossila Four-point-probe (model no. T2001A4) and analyzed with sheet resistance measurement software from Ossila. Minimum 4 different replicates of each were measured for to ensure reproducibility.

4.2.8 | Preparation and Characterization of DSSCs

FTO glass substrates were cleaned following 15 min steps with Derquim soap solution, deionized water and isopropanol each in an ultrasonication bath. The substrates were gently dried in nitrogen gas flow and further treated with UV-ozone cleaner (Model No. 256–220, Jelight Company, 20 min). The cleaned FTO glasses were immersed in a 0.4 mM aqueous $TiCl_4$ solution (Titanium (IV) chloride solution, 0.09 M in 20% HCl) at 70°C for 30 min and washed with water and ethanol, followed by nitrogen blow drying and annealing at 450°C for 30 minutes.

TiO_2 paste was doctor bladed using a circular scotch tape with 0.196 cm^2 active area on the cleaned and pre-treated FTO glass and dried at 125°C for 6 min. The electrodes were sintered according to the following: 325°C for 5 min, 375°C for 5 min, 450°C for 15 min, 500°C for 15 min. The prepared TiO_2 film electrodes were further treated in 0.4 mM aqueous $TiCl_4$ solution at 70°C for 30 min and washed with water and ethanol, followed by nitrogen blow drying and annealing at 500°C for 90 minutes. Upon post treatment, the TiO_2 electrodes were immersed in D131 0.5 mM solution (1:1 volume for acetonitrile:4-tert butanol) for 24 h.

The liquid water-based electrolyte was prepared by dissolving 5 M NaI, 25 mM I_2 in deionized water saturated with chenodeoxycholic acid (stirring DI water with CDCA overnight followed by filtering). Few drops of electrolyte solution were placed before closing the device with different counter-electrodes using a thermoplastic polyamide heat-resistant bi-adhesive tape. The current–voltage (*J–V*) measurements of the DSSCs were carried with Solar Simulator, Sol3A Class AAA (450 W Xenon-lamp; Newport) calibrated with a KG5-filtered Silicon reference cell (Newport/Oriel, Model 91150 V). *J–V* curves were recorded in the range of 0–1.0 V with a scan rate of 0.1 V s^{-1} using a potentiostat (PGSTAT204, Metrohm Autolab) at standard 1 sun AM M1.5G illumination. The final solar cell layout is reported in Figure S8b.

Author Contributions

Elena Palmieri: conceptualization, data curation, formal analysis, investigation, writing – original draft preparation, and writing – reviewing & editing. **Sara Ferrara**: conceptualization, data curation, formal analysis, investigation, writing – original draft preparation, and writing – reviewing & editing. **Sanchari Chowdhury**: conceptualization, data curation, formal analysis, investigation, writing – original draft preparation, and writing – reviewing & editing. **Luca Montaina**: investigation. **Claudia Mazzuca**: formal analysis and writing – reviewing & editing. **Francesco Maita**: conceptualization, supervision, investigation, and writing – reviewing & editing. **Ruben D. Costa**: conceptualization and writing – reviewing & editing. **Luca Maiolo**: conceptualization, supervision, investigation, and writing – reviewing & editing.

Acknowledgements

This work was funded by Ministero delle Imprese e del Made in Italy (MIMIT) under IPCEI Microelettronica 2, project MicroTech_for_Green. The authors would like to thank Dott.ssa Adele De Ninno and Dott. Enrico Verona for the contribution in the preparation of the Ti and Pt sputtered samples.

Open access publishing facilitated by Consiglio Nazionale delle Ricerche, as part of the Wiley - CRUI-CARE agreement.

Conflicts of Interest

The authors declare no conflicts of interest.

Data Availability Statement

The data that support the findings of this study are available from the corresponding author upon reasonable request.

References

1. 2050 European Technology, I. P. for Photovoltaics, Solar LCOE may decrease by up to 20% in Europe by 2030, 2023, https://www.pv-magazine.com/2023/12/14/solar-lcoe-may-decrease-by-up-to-20-in-europe-by-2030/.

2. P. Jowett, Solar generation grew by 30% in 2024, says IEA, 2025, https://www.pv-magazine.com/2025/02/20/solar-generation-grew-by-30-in-2024-says-iea/.

3. IEA, *Solar*, accessed July 30, 2025, https://www.iea.org/energy-system/renewables/solar-pv.

4. A. Machín and F. Márquez, "Advancements in Photovoltaic Cell Materials: Silicon, Organic, and Perovskite Solar Cells," *Materials* 17 (2024): 1165.

5. N. S. Seroka, R. Taziwa, and L. Khotseng, "Solar Energy Materials-Evolution and Niche Applications: A Literature Review," *Materials* 15 (2022): 5338.

6. N. K. Farhana, N. M. Saidi, S. Bashir, S. Ramesh, and K. Ramesh, "Review on the Revolution of Polymer Electrolytes for Dye-Sensitized Solar Cells," *Energy & Fuels* 35 (2021): 19320–19350.

7. K. A. Pishro and M. H. Gonzalez, "Use of Deep Eutectic Solvents in Environmentally-Friendly Dye-Sensitized Solar Cells and Their Physicochemical Properties: a Brief Review," *RSC Advances* 14 (2024): 14480–14504.

8. J. C. de Haro, E. Tatsi, L. Fagiolari, et al., "Lignin-Based Polymer Electrolyte Membranes for Sustainable Aqueous Dye-Sensitized Solar Cells," *ACS Sustainable Chemistry & Engineering* 9 (2021): 8550–8560.

9. S. Mahalingam, A. Nugroho, D. Floresyona, et al., "Bio and Non-Bio Materials-Based Quasi-Solid State Electrolytes in DSSC: A Review," *International Journal of Energy Research* 46 (2022): 5399–5422.

10. S. Rahman, A. Haleem, M. Siddiq, et al., "Research on Dye Sensitized Solar Cells: Recent Advancement toward the Various Constituents of Dye Sensitized Solar Cells for Efficiency Enhancement and Future Prospects," *RSC Advances* 13 (2023): 19508–19529.

11. P. Li, W. Wang, H. Li, et al., "Foldable Solar Cells: Structure Design and Flexible Materials," *Nano Select* 2 (2021): 865–879.

12. E. Dauzon, X. Sallenave, C. Plesse, F. Goubard, A. Amassian, and T. D. Anthopoulos, "Pushing the Limits of Flexibility and Stretchability of Solar Cells: a Review," *Advanced Materials* 33 (2021): 2101469.

14392054, 2026, 7, Downloaded from https://onlinelibrary.wiley.com/doi/10.1002/mame.202500434 by CochraneItalia, Wiley Online Library on [22/10/2026]. See the Terms and Conditions (https://onlinelibrary.wiley.com/terms-and-conditions) on Wiley Online Library for rules of use; OA articles are governed by the applicable Creative Commons License

13. Y. Sun, T. Liu, Y. Kan, K. Gao, B. Tang, and Y. Li, "Flexible Organic Solar Cells: Progress and Challenges," *Small Science* 1 (2021): 2100001.

14. B. K. Korir, J. K. Kibet, and S. M. Ngari, "A Review on the Current Status of Dye-Sensitized Solar Cells: Toward Sustainable Energy," *Energy Science & Engineering* 12 (2024): 3188–3226.

15. E. Palmieri, R. Cancelliere, F. Maita, L. Micheli, and L. Maiolo, "An Ethyl Cellulose Novel Biodegradable Flexible Substrate Material for Sustainable Screen-Printing," *RSC Advances* 14 (2024): 18103–18108.

16. E. Palmieri, F. Maita, I. Lucarini, J. I. D. R. De Vicente, A. Minotti, and L. Maiolo, "Sustainable Space Agriculture: Biodegradable Sensors Redefining Greenhouse Monitoring Beyond Earth," in Proceedings of the 2024 IEEE 11th International Workshop on Metrology for AeroSpace (MetroAeroSpace) (IEEE, 2024), 417–421.

17. E. Palmieri, F. Maita, A. Pellegrino, G. Avola, M. Distefano, and L. Maiolo, "Revolutionizing Precision Agriculture: Exploring a Novel Biodegradable Substrate for Advanced Electronic Sensors," in Proceedings of the 2023 IEEE International Workshop on Metrology for Agriculture and Forestry (MetroAgriFor) (IEEE, 2023), 763.

18. E. Luoma, M. Välimäki, J. Ollila, K. Heikkinen, and K. Immonen, "Bio-Based Polymeric Substrates for Printed Hybrid Electronics," *Polymers* 14 (2022): 1863.

19. C. P. Teng, M. Y. Tan, J. P. W. Toh, et al., "Advances in Cellulose-Based Composites for Energy Applications," *Materials* 16 (2023): 3856.

20. Z. Xiao, S. Li, J. Liu, et al., "Ecofriendly Cellulose Substrate-Based Flexible Transparent Electrode for Flexible Organic Solar Cells with Efficiency over 18%," *Solar RRL* 8 (2024): 2400206.

21. L. Huang, Y. Li, Z. Zheng, Y. Bai, T. P. Russell, and C. He, "Flexible, Transparent, and Sustainable Cellulose-Based Films for Organic Solar Cell Substrates," *Materials Horizons* 11 (2024): 1560–1566.

22. S. V. Costa, P. Pingel, S. Janietz, and A. F. Nogueira, "Inverted Organic Solar Cells Using Nanocellulose as Substrate," *Journal of Applied Polymer Science* 133 (2016): 43679.

23. A. Operamolla, "Renewable and Biodegradable Cellulose Nanopaper Substrates for Transparent Light-Harvesting Devices: Interaction with Humid Environment," *International Journal of Photoenergy* 2019 (2019): 3057929.

24. L. Hu, G. Zheng, J. Yao, et al., "Transparent and Conductive Paper from Nanocellulose Fibers," *Energy & Environmental Science* 6 (2013): 513–518.

25. J. Wu, X. Che, H. Hu, et al., "Organic Solar Cells Based on Cellulose Nanopaper from Agroforestry Residues with an Efficiency of over 16% and Effectively Wide-Angle Light Capturing," *Journal of Materials Chemistry A* 8 (2020): 5442–5448.

26. H. Zhu, Y. Li, Z. Fang, et al., "Highly Thermally Conductive Papers with Percolative Layered Boron Nitride Nanosheets," *ACS Nano* 8 (2014): 3606–3613.

27. L. Gao, L. Chao, M. Hou, et al., "Flexible, Transparent Nanocellulose Paper-Based Perovskite Solar Cells," *npj Flexible Electronics* 3 (2019): 4.

28. M. Nogi, M. Karakawa, N. Komoda, H. Yagyu, and T. T. Nge, "Transparent Conductive Nanofiber Paper for Foldable Solar Cells," *Scientific Reports* 5 (2015): 17254.

29. H. Pervaiz, Z. S. Khan, N. Shahzad, G. Ali, N. Iqbal, and S. Javed, "Fabrication of Cellulose Paper-Based Counter Electrodes for Flexible Dye-Sensitized Solar Cells," *Physical Chemistry Chemical Physics* 25 (2023): 428–438.

30. J. Wu, Z. Lan, J. Lin, et al., "Counter Electrodes in Dye-Sensitized Solar Cells," *Chemical Society Reviews* 46 (2017): 5975–6023.

31. J. Li, H. Yang, K. Huang, et al., "Conductive Regenerated Cellulose Film as Counter Electrode for Efficient Dye-Sensitized Solar Cells," *Cellulose* 25 (2018): 5113–5122, https://doi.org/10.1007/s10570-018-1913-1.

32. F. Bella, S. Galliano, M. Falco, et al., "Unveiling Iodine-Based Electrolytes Chemistry in Aqueous Dye-Sensitized Solar Cells," *Chemical Science* 7 (2016): 4880–4890.

33. E. Palmieri, L. Maiolo, I. Lucarini, et al., "Toward Sustainable Electronics: Exploiting the Potential of a Biodegradable Cellulose Blend for Photolithographic Processes and Eco-Friendly Devices," *Advanced Materials Technologies* 9 (2024): 2301282.

34. Y. Cheng, X. Ren, G. Gao, and L. Duan, "High Strength, Anti-Freezing and Strain Sensing Carboxymethyl Cellulose-Based Organohydrogel," *Carbohydrate Polymers* 223 (2019): 115051.

35. A. Porfyris, S. Vasilakos, C. Zotiadis, et al., "Accelerated Ageing and Hydrolytic Stabilization of Poly(lactic acid) (PLA) under Humidity and Temperature Conditioning," *Polymer Testing* 68 (2018): 315–332.

36. J. Li, X. Du, A. Zhang, et al., "Hydrogen-Bonded Polymeric Materials with High Mechanical Properties and High Self-Healing Capacity," *Materials Chemistry Frontiers* 8 (2024): 3828–3858.

37. G. Stojkov, Z. Niyazov, F. Picchioni, and R. K. Bose, "Relationship between Structure and Rheology of Hydrogels for Various Applications," *Gels* 7 (2021): 255.

38. R. V. Barrulas and M. C. Corvo, "Rheology in Product Development: An Insight into 3D Printing of Hydrogels and Aerogels," *Gels* 9 (2023): 986.

39. T. Wang, S. Liu, and J. Tsai, "Micromechanical Stick-Slip Model for Characterizing Damping Responses of Single-Walled Carbon Nanotube Nanocomposites," *Journal of Composite Materials* 50 (2016): 57–73.

40. A. Naderi, A. Koschella, T. Heinze, et al., "Sulfoethylated Nanofibrillated Cellulose: Production and Properties," *Carbohydrate Polymers* 169 (2017): 515–523.

41. T. G. Mezger, *The Rheology Handbook* (Vincentz Network, 2006).

42. I. Leppänen, M. Vikman, A. Harlin, and H. Orelma, "Enzymatic Degradation and Pilot-Scale Composting of Cellulose-Based Films with Different Chemical Structures," *Journal of Polymers and the Environment* 28 (2020): 458–470.

43. N. Yadav and M. Hakkarainen, "Degradable or Not? Cellulose Acetate as a Model for Complicated Interplay between Structure, Environment and Degradation," *Chemosphere* 265 (2021): 128731.

44. L. Filiciotto and G. Rothenberg, "Biodegradable Plastics: Standards, Policies, and Impacts," *Chemsuschem* 14 (2021): 56–72.

45. V. Bauchmüller, M. Carus, L. Dammer, et al., *BioSinn – Products for which biodegradation makes sense*, 2021, https://renewable-carbon.eu/publications/product/biosinn-products-for-which-biodegradation-makes-sense-pdf/.

46. M. Shandilya, S. Thakur, and S. Thakur, "Magnetic Amendment in the Fabrication of Environment Friendly and Biodegradable Iron Oxide/Ethyl Cellulose Nanocomposite Membrane via Electrospinning," *Cellulose* 27 (2020): 10007–10017.

47. N. M. Kuznetsov, A. A. Zakharevich, A. Y. Vdovichenko, et al., "Highly Porous Particles of Cellulose Derivatives for Advanced Applications," *ChemPlusChem* 89 (2024): 202400375.

48. K. K. Khichar, S. B. Dangi, V. Dhayal, et al., "Structural, Optical, and Surface Morphological Studies of Ethyl Cellulose/Graphene Oxide Nanocomposites," *Polymer Composites* 41 (2020): 2792–2802.

49. K. K. Pandey and A. J. Pitman, "FTIR Studies of the Changes in Wood Chemistry Following Decay by Brown-Rot and White-Rot Fungi," *International Biodeterioration & Biodegradation* 52 (2003): 151–160.

50. C. Mazzuca, L. Severini, M. Missori, et al., "Evaluating the Influence of Paper Characteristics on the Efficacy of New Poly(vinyl alcohol) Based Hydrogels for Cleaning Modern and Ancient Paper," *Microchemical Journal* 155 (2020): 104716.

51. J. Łojewska, A. Lubańska, P. Miśkowiec, T. Łojewski, and L. M. Proniewicz, "FTIR In Situ Transmission Studies on the Kinetics of Paper Degradation via Hydrolytic and Oxidative Reaction Paths," *Applied Physics A* 83 (2006): 597–603.

14392054, 2026, 7, Downloaded from https://onlinelibrary.wiley.com/doi/10.1002/mame.202500434 by CochraneItalia, Wiley Online Library on [22/10/2026]. See the Terms and Conditions (https://onlinelibrary.wiley.com/terms-and-conditions) on Wiley Online Library for rules of use; OA articles are governed by the applicable Creative Commons License

52. A. Mosca Conte, O. Pulci, A. Knapik, et al., "Role of Cellulose Oxidation in the Yellowing of Ancient Paper," *Physical Review Letters* 108 (2012): 158301.

53. P. Calvini and A. Gorassini, "FTIR – Deconvolution Spectra of Paper Documents," *Restaurator* 23 (2002): 48–66.

54. M. E. Fuller, C. Andaya, and K. McClay, "Evaluation of ATR-FTIR for Analysis of Bacterial Cellulose Impurities," *Journal of Microbiological Methods* 144 (2018): 145–151.

55. S. A. Tatulian, "Structural Characterization of Membrane Proteins and Peptides by FTIR and ATR-FTIR Spectroscopy," *Methods in Molecular Biology* 974 (2013): 177–218.

56. E. Palmieri, A. Alabiso, L. Migliore, et al., "Enhancing Stability: The Protective Role of Nanodiamonds against Biodegradation in Cellulose Ethers Dispersions," *Polymer Degradation and Stability* 234 (2025): 111247.

57. R. S. R. Kananke Udubokke Rathnayakage, T. M. W. J. Bandara, K. Wijayaratne, G. R. A. Kumara, L. A. de Silva, and K. Tennakone, "Fluorine-Doped Tin Oxide Thin Films with High Surface Conductance and Low Transparency for Boosting Performance in Dye-Sensitized Solar Cell Applications," *ACS Applied Energy Materials* 6 (2023): 8336–8348.

58. P. Gemeiner, N. Perinka, L. Svorc, et al., "Pt–Free Counter Electrodes Based on Modified Screen–Printed PEDOT:PSS Catalytic Layers for Dye–Sensitized Solar Cells," *Materials Science in Semiconductor Processing* 66 (2017): 162–169.

59. B. Anothumakkool, I. Agrawal, S. N. Bhange, et al., "Pt- and TCO-Free Flexible Cathode for DSSC from Highly Conducting and Flexible PEDOT Paper Prepared via in Situ Interfacial Polymerization," *ACS Applied Materials & Interfaces* 8 (2016): 553–562.

60. J. Pringle, V. Armel, and D. Macfarlane, "Electrodeposited PEDOT-on-Plastic Cathodes for Dye-Sensitized Solar Cells," *Chemical Communications* 46 (2010): 5367.

61. J. An, W. Guo, and T. Ma, "Enhanced Photoconversion Efficiency of all-Flexible Dye-Sensitized Solar Cells Based on a Ti Substrate with TiO_2 Nanoforest Underlayer," *Small* 8 (2012): 3427–3431.

62. S. Cherng, C. Chen, W. Dow, C. Lin, and S. Chen, "Chemical Deposition of Ni/Pt Bi-Layer on Polyimide Film as Flexible Counterelectrodes for Dye-Sensitized Solar Cells," *Electrochemical and Solid-State Letters* 14 (2011): P13–P15.

63. Y. Zhu, C. Gao, Q. Han, et al., "Large-Scale High-Efficiency Dye-Sensitized Solar Cells Based on a Pt/Carbon Spheres Composite Catalyst as a Flexible Counter Electrode," *Journal of Catalysis* 346 (2017): 62–69.

64. B. L. da Silva, D. T. Cestarolli, and E. M. Guerra, "Development of Flexible Dye-Sensitized Solar Cells Based on Natural Dyes: Optical Properties of V_2O_5 Xerogel and Polyaniline," *Optical Materials* 174 (2026): 118027.

65. H. Lee, J. Kim, D. Y. Kim, and Y. Seo, "Co-Sensitization of Metal Free Organic Dyes in Flexible Dye Sensitized Solar Cells," *Organic Electronics* 52 (2018): 103–109.

66. Q. Xu, M. Li, P. Yan, et al., "Polypyrrole-Coated Cotton Fabrics Prepared by Electrochemical Polymerization as Textile Counter Electrode for Dye-Sensitized Solar Cells," *Organic Electronics* 29 (2016): 107–113.

67. B. Li, F. Huang, J. Zhong, J. Xie, M. Wen, and Y. Peng, "Fabrication of Flexible Dye-Sensitized Solar Cell Modules Using Commercially Available Materials," *Energy Technology* 4 (2016): 536–542.

68. H. Pervaiz, N. Shahzad, Q. Jamil, and M. I. Shahzad, "Electrochemical and Power Conversion Performance of Different Counter Electrode Materials for Flexible Dye-Sensitized Solar Cells," *RSC Advances* 13 (2023): 20255–20263.

69. F. C. Tavares, J. M. Luzardo, A. A. Dias, R. Valaski, J. R. Araújo, and R. Jakomin, "Strong and Flexible Platinum-Free Counter Electrode for DSSC Applications," *Journal of Applied Polymer Science* 143, no. 3 (2026): e58064, https://doi.org/10.1002/app.58064.

70. K. S. Vinod, R. Thangavel, S. R. Reshma, V. Narayanan, and K. S. Rajni, "Reduced Graphene Oxide Coated Cotton Fabric as Flexible Counter Electrode for Dye Sensitized Solar Cell Applications," *Next Materials* 10 (2026): 101457.

Supporting Information

Additional supporting information can be found online in the Supporting Information section.

Supporting File: mame70241-sup-0001-SuppMat.docx.

14392054, 2026, 7, Downloaded from https://onlinelibrary.wiley.com/doi/10.1002/mame.202500434 by CochraneItalia, Wiley Online Library on [22/10/2026]. See the Terms and Conditions (https://onlinelibrary.wiley.com/terms-and-conditions) on Wiley Online Library for rules of use; OA articles are governed by the applicable Creative Commons License